

## The hard X-ray emission along the “Z” track in GX 17+2

G. Q. Ding<sup>1,\*</sup> & C. P. Huang<sup>1</sup>

<sup>1</sup>*Xinjiang Astronomical Observatory, CAS, 150 Science 1-Street, Urumqi 830011, China*

\**e-mail: dinggq@xao.ac.cn, dinggq@gmail.com*

2018 October 28

**Abstract.** Using the data from the Proportional Counter Array (PCA) and the High-Energy X-ray Timing Experiment (HEXTE) on board *Rossi X-Ray Timing Explorer* for Z source GX 17+2, we investigate the evolution of its PCA spectra and HEXTE spectra along a “Z” track on its hardness-intensity diagram. A hard X-ray tail is detected in the HEXTE spectra. The detected hard X-ray tails are discontinuously scattered throughout the “Z” track. The found hard tail hardens from the horizontal branch, through the normal branch, to the flaring branch in principle and it contributes  $\sim(20-50)\%$  of the total flux in 20-200 keV. Our joint fitting results of the PCA+HEXTE spectra in 3-200 keV show that the portion of Comptonization in the bulk-motion Comptonization (BMC) model accounts for the hard X-ray tail, which indicates that the BMC process could be responsible for the detected hard tail. The temperature of the seed photons for BMC is  $\sim 2.7$  keV, implying that these seed photons might be emitted from the surface of the neutron star (NS) or the boundary layer between the NS and the disk and, therefore, this process could take place around the NS or in the boundary layer.

*Key words:* accretion, accretion disks – X-rays: binaries – stars: individual (GX 17+2) – stars: neutron

### 1. Introduction

In the past several decades, the huge numbers of data from X-ray satellites make it possible to deeply investigate the spectra of X-ray binaries, including black holes X-ray binaries (BHXBs) and neutron star X-ray binaries (NSXBs). Usually, the hard X-ray tails, i.e. the X-ray spectra higher than dozens of keV, e.g. above  $\sim 40$  keV, have been observed in BHXBs. It is a nature assumption that the hard tails are resulted from Comptonization of seed photons by high-energy electrons. In BHXBs, the high-energy electrons exist in two scenarios (see review of Done et al. 2007). In the hard states of BHXBs, the energetic electrons are assumed to exist in the optically thin part between the black hole and an optically thick truncated disk far from the black hole, where the high-energy electrons are thermalized and share Maxwellian distribution, and the emitting spectrum can be described by thermal Comptonization in which the soft photons from the disk are inversely Comptonized by these thermal electrons (Shapiro et al. 1976; Sunyaev & Truemper 1979; Sunyaev & Titarchuk 1980; Titarchuk 1994). While, in the soft states the high-energy electrons are described by a “Hybrid” distribution, i.e. a mixture with thermal distribution and non-thermal power-law (PL) distribution (Poutanen & Coppi 1998; Coppi 1999; Gierliński et al. 1999; Zdziarski et al. 2001); the thermal electrons might come from

the remains of the hot inner flow and the non-thermal electrons might originate from the magnetic flares above the disk (Done et al. 2007). Another alternative mechanism for generation of hard X-ray tails in BHXBs is the bulk-motion Comptonization (BMC), in which the seed photons are inversely Comptonized by the electrons which freely fall with relativistic speed onto the black holes (Titarchuk et al. 1997; Laurent & Titarchuk 1999).

NSXBs are divided into two types, i.e. atoll sources and Z sources (Hasinger & van der Klis 1989). The hard X-ray tails have been detected in a few atoll sources. The presence of a PL hard tail in the broadband spectra of atoll sources can trace back to such detection from the *BeppoSAX* observations for 4U 0614+091 (Piraino et al. 1999). With *INTEGRAL* observations, Paizis et al. (2006) detected a hard tail in GX 13+1, which makes it the first atoll source with a hard tail. Then, this non-thermal PL hard tail with  $\Gamma=2.76$  was detected in the *INTEGRAL* spectrum of 4U 1636-53 during its soft state (Fiocchi et al. 2006). A PL hard tail with photon index of  $\sim 2.4$  was also found in the *INTEGRAL* spectrum of 4U 1820-30 during its island state (IS) (Tarana et al. 2007). Afterward, the similar hard tail having a photon index ( $\Gamma$ )  $\sim 2.9$  and contributing  $\sim 11\%$  of the total flux in the 0.1-200 keV energy interval was detected in 4U 1705-44 from a *BeppoSAX* observation (Piraina et al. 2007). With the observations of *Suzaku* and *Rossi X-Ray Timing Explorer (RXTE)*, such high-energy X-ray tail was detected in Aql X-1 too (Raichur et al. 2011), also found in the *INTEGRAL* spectrum of another atoll source 4U 1728-34 (Tarana et al. 2011). Although some models have been proposed to explain the detected hard X-ray tails in atoll sources, there has no a unified explanation. Paizis et al. (2006) used the generic Comptonization model, i.e. the BMC model, to fit the spectrum of GX 13+1 in  $\sim(20-80)$  keV and got statistically good fitting, indicating that the BMC process could be an alternative mechanism for producing the hard X-ray emission in this source. Due to the high ratio of the radio flux to the peak X-ray flux found in 4U 1636-53, Fiocchi et al. (2006) considered that the synchrotron emission in the jet could be responsible for the detected hard tail. However, in order to explain the high-energy X-ray tails in 4U 1820-30 and 4U 1728-34, Tarana et al. (2007, 2011) proposed that the emission of non-thermal electrons in a hybrid plasma might be the origin of the detected hard X-ray tails.

However, the detection of hard X-ray tails in Z sources is unpredictable and the detected hard tails present complicated behaviors. Generally, among the Z sources, the hard tail is detected on the horizontal branch (HB) and it gradually fades away as they moves along the “Z” track on their hardness-intensity diagrams (HIDs) (Di Salvo et al. 2000, 2002; Lin et al. 2009; Ding et al. 2003, 2011). But, occasionally, the hard X-ray emission is not correlated with the positions on the HIDs (D’Amico et al. 2001). Analyzing the spectra of High-Energy X-ray Timing Experiment (HEXTE) on board *RXTE*, D’Amico et al. (2001) found that the PL hard X-ray tail of Sco X-1 hardens in the sequence HB $\rightarrow$ NB $\rightarrow$ FB on its HID. Using the *RXTE* observations for Sco X-1, D’Aí et al. (2007) studied the evolution of broadband spectra (3-200 keV) of Sco X-1 on its color-color diagram (CD) and proposed the “Hybrid” Comptonization model to explain the hard X-ray emission. With *INTEGRAL* observation, Revnivtsev et al. (2014) investigated the hard tail of Sco X-1. Analyzing the broadband spectra (0.1-200 keV) of a *BeppoSAX* observation for GX 349+2, Di Salvo et al. (2001) detected a hard tail with photon index  $\sim 2$ . A hard X-ray tail of GX 340+0 was also detected in its *BeppoSAX* spectra (Lavagetto et al. 2004). Using the *BeppoSAX* observations for Cir X-1, which hosts an elliptical orbit with high eccentricity ( $e \sim 0.7-0.9$ ), Iaria et al. (2001, 2002) studied its broadband spectra near the periastron (orbital phase 0) or at the orbital phases close to the apoastron (orbital phase 0.5) and detected similar hard X-ray tails with photon index  $\sim 3.2$  during the two

orbital episodes. Interestingly, analyzing *RXTE* data, Ding et al. (2006b) found orbital modulation for the hard X-ray emission of Cir X-1. In this peculiar source, from the periastron to the apastron, the PL hard tail softens and its flux increases, and, however, from the apastron to the next periastron (orbital phase 1), it hardens and its flux increases.

The origin of hard tails in Z sources is debated. Some models have been proposed for the production of hard X-ray emission in Z sources. Z sources share neutron star (NS) surface magnetic field strength of  $\sim 10^9$  G (Fock 1996; Ding et al. 2006b, 2011), so synchrotron emission of energetic electrons might be an origin (Riegler 1970; D’Amico et al. 2001; Iaria et al. 2002). Di Salvo et al. (2006) proposed the “Hybrid” model for the production of hard tails in Z sources. In the “Hybrid” model, the high-energy electrons are from a hybrid thermal/nonthermal corona. A jet might be another origin of hard tails in Z sources due to the fact that in these sources both the hard X-ray emission flux and radio flux are highest on the HB, then fade away along the “Z” track on their HIDs, and, finally, become lowest on the flaring branch (FB) (Penninx et al. 1988; Di Salvo et al. 2000, 2002; Lin et al. 2009; Ding et al. 2003, 2011; Migliari et al. 2007; Fender et al. 2007).

It is noted that for the past about ten years the BMC model has been considered for the production of hard tails in Z sources. Paizis et al. (2006) used this model to fit the broadband spectra of NSXBs for the first time, then Farinelli et al. (2007, 2008, 2009) developed this model and used it to fit the broadband spectra of Z sources. Ding et al. (2011) used the model to fit the broadband spectra of the transient Z source XTE J1701-462 and suggested that the bulk-motion Comptonization near the NS could be an alternative mechanism for producing the hard tails in this source.

In this work, using the data from the Proportional Counter Array (PCA) and the HEXTE on board *RXTE* satellite for Z source GX 17+2, we study the evolution of its PCA spectra and HEXTE spectra along a “Z” track on its HID. We detect the hard X-ray tails in its HEXTE spectra and investigate the possible mechanism for producing the hard X-ray emission. We describe our data analysis in Section 2, present and discuss our results in Section 3, and give our conclusion in Section 4.

## 2. Data analysis

### 2.1 The selected observations

Using software HEASOFT 6.11 and FTOOLS V6.11, we select the *RXTE* observations for GX 17+2 between 1999 Oct. 3 and Oct. 12, a total of  $\sim 297.6$  ks, to perform our analysis. The “Standard 2” mode data with a time resolution of 16 s are used to produce the color-color diagram (CD) and the HID. The two proportional counter units (PCUs 0, 2) are used because they are always on. Following Homan et al. (2002), the soft color is defined as the count rate ratio between the [4.6-7.1 keV (channels 8-13)] and [2.9-4.6 keV (channels 4-7)] energy bands, and the hard color as that between the [10.5-19.6 keV (channels 22-42)] and [7.1-10.5 keV (channels 14-21)] energy bands, and intensity as the count rate covering the energy range [2.9-19.6 keV (channels 4-42)]. Using “Standard 2” mode data, applying FTOOLS SAEXTRACT, we extract the source light curves. Then, using the background model provided by *RXTE* team and applying RUNPCABACKEST, a tool of FTOOLS, we produce the background files and thus extract the background light curves. Finally, we obtain the background-subtracted light curves with various energy bands and create the CD and HID by using FTOOLS LCURVE, which are shown by Figure 1 and Figure 2, respectively, presenting complete “Z” tracks, respectively. From the top left to bottom right on the CD, the track is divided into three segments which are called HB, normal branch (NB), and FB, respectively. These branches are correspondingly demonstrated on

the HID (Figure 2). We split the “Z” track on the HID into 17 regions in order to minimize count rate variations in each region and then extract the PCA and HEXTE spectra of each of the 17 regions. In Figure 2, the HB, NB, and FB consist of regions 1–4, regions 5–9, and regions 10–17, respectively.

## 2.2 Extracting the spectra

Firstly, according to the hard color and intensity of each region in Figure 2, we determine its absolute time interval. Then, using SAEXTRCT, we extract the PCA and HEXTE spectra of each region on the “Z” track by confining the time interval. The “Standard 2” mode data from PCUs 0, 2, providing count spectra each 16 s in 129 energy channels covering 2–100 keV, are used to generate the PCA spectra. Using RUNPCABACKEST and applying the background model provided by *RXTE* team, we produce the PCA background files and, thus, the background spectra and background-subtracted spectra of PCA are generated. For HEXTE, we also use the standard mode data, providing 64 channel count spectra each 16 s covering 10–250 keV range, to perform spectral analysis. HEXTE comprises two clusters, cluster A and cluster B, each of which consists of four detectors. We only use the data from cluster A, because detector 2 of cluster B loses its spectral capability and automatic gain control after 1996 Mar. 6<sup>1</sup>. FTOOLS HXTBACK is used to separate the background data from the source+background data in raw FITS files, then the source and background HEXTE spectra are extracted, and the deadtimes of these spectra are corrected with command HXTDEAD. Finally, the background-subtracted spectra of HEXTE are obtained. In order to improve the signal-to-noise ratios (S/Ns) of HEXTE spectra, we rebin the HEXTE spectra for per new bin to have S/Ns larger than 1.5. When extracting spectra, Good Time Interval (GTI) files are applied, which are created by FTOOLS MAKETIME following the criteria: the offset between the source and telescope pointing direction is less than 0.02° and the elevation above the Earth’s limb is greater than 10°.

## 2.3 The BMC model

Titarchuk et al. (1996, 1997) and Laurent & Titarchuk (1999) studied the Compton up-scattering of soft X-ray photons in a converging flow onto a compact star and suggested that the bulk-motion of the converging flow is significant in up-scattering photons and then the bulk-motion Comptonization might be responsible for the PL spectra seen in X-ray sources. Using observational data from the *Compton Gamma Ray Observatory*, *CGRO* and *RXTE*, Shrader & Titarchuk (1998) and Titarchuk & Seifina (2009) investigated the bulk-motion Comptonization in BHXBs and found that this kind of Comptonization does exist in BHXBs. In XSPEC, the bulk-motion Comptonization is described by the bmc model and expressed as:

$$F(E) = \frac{C_N}{1+A} (BB + A \times BB * G). \quad (1)$$

This expression consists of two components: one is the injected blackbody-like spectrum (BB), and the other is  $BB * G$ , a convolution of BB with Green’s function  $G(E, E_0)$ , which accounts for the observed Comptonization component. This model includes four parameters: the temperature of the seed photons  $kT_{\text{bb}}$ , spectral index  $\alpha$  (photon index  $\Gamma = \alpha + 1$ ), a logarithm of the weighting factor  $\log(A)$ , and the normalization  $C_N$ . The

<sup>1</sup><http://heasarc.gsfc.nasa.gov/docs/xte/recipes/hexte.html>

factor  $1/(1 + A)$  is the fraction of the seed photon radiation which is not affected by a noticeable up-scattering in the plasma cloud and seen directly by the Earth observer, whereas the Comptonization factor  $f$  ( $f = A/(1 + A)$ ) is the fraction of the seed photon radiation which is up-scattered by the Compton cloud. High values of  $\alpha$  indicate the low efficiency of Comptonization that usually occurs when the thermal equilibrium between the Compton cloud and the seed photon environment is established. In two cases, the BMC model is reduced to the BB model: one is with  $A \ll 1$ , indicating that the convolution Comptonization component is negligible; the other is with  $A \gg 1$  &  $\alpha \gg 1$ , meaning that near all the seed photons are up-scattered by the Compton cloud and, however the efficiency of Comptonization is small.

#### 2.4 Spectral fitting

The Eastern and Western models have been two classical spectral models for NSXBs (Mitsuda et al. 1984, 1989; White et al. 1986, 1988). Church & Bałucińska-Church (1995, 2004) developed the two models into an extended accretion disk corona (ADC) model which consists of a blackbody (BB) interpreted as the emission from the NS surface and a cut off powerlaw (CPL) representing the Comptonization of the soft photons from the disk by the energetic electrons from an extend ADC above the disk. The extended ADC model was used to fit the PCA spectra of Z sources (Church et al. 2006, 2012; Jackson et al. 2009; Bałucińska-Church et al. 2010). In this work, we accept this model. Taking into account the Fe- $K_\alpha$  emission, we use a combination model of BB+LINE+CPL to fit the 17 PCA spectra in 3-30 keV. Di Salvo et al. (2000) detected an absorption edge at  $\sim 8.5$  keV in the broadband *BeppoSAX* spectra of GX 17+2. In our practice, a unusual structure is presented in  $\sim(8-10)$  keV in the residual distribution when we use the BB+LINE+CPL model to fit the PCA spectra. If an absorption edge is added into the model, the fitting can be improved, so it is also taken into account in our fitting. Certainly, the interstellar absorption is taken into consideration and, however, the lack of data below  $\sim 3$  keV prevents XSPEC from determining the photoelectric interstellar hydrogen column density ( $N_H$ ). But, the values of ( $N_H$ ) is larger than  $3 \times 10^{22}$  atom  $\text{cm}^{-2}$  when the extended ADC model is used to fit the PCA spectra of Z sources except Sco X-1 (Church et al. 2006, 2012; Jackson et al. 2009; Bałucińska-Church et al. 2010), so the PCA spectra is feasible to measure the values of  $N_H$  of these Z sources. Due to the calibration uncertainties, a systematic error of 0.5% is added into the PCA spectra (Barret et al. 2000). The PCA response matrixes are created with *RXTE* perl script PCARSP and the spectra are fitted with XSPEC version 12.7.0. The fitting results are listed in Table 1 and six unfolded spectra are shown in Figure 3.

The HEXTE response matrix of Cluster A (xh97mar20c\_pwa\_64b.rmf) and the ancillary response file of Cluster A (hexte\_00may26\_pwa.arf) provided by *RXTE* team are applied when the HXTE spectra are fitted. Using a two-component model consisting of a thermal bremsstrahlung (BREMSS) and a simple PL, D'Amico et al. (2001) fit the HEXTE spectra of Sco X-1 in which a hard tail was detected. In this work, we use this two-component model or a single-component model, i.e. the BREMSS model, to fit the 17 HEXTE spectra in 20-200 keV. We use the XSPEC convolution model CFLUX to calculate the unabsorbed flux of BREMSS in 20-50 keV and the unabsorbed flux of PL in 20-200 keV. The fitting results are listed in Table 2 and some unfolded spectra are shown in Figures 4-6.

We jointly fit six PCA+HEXTE spectra in 3-200 keV with a combination model consisting of a BMC, a LINE, and a CPL. A multiplicative constant is added to the spectral model for allowing the HEXTE spectral normalization to float with the PCA spectral nor-

malization. In our practice, we fix this constant at 1 for the PCA spectra, while it is free for the HEXTE spectra, varying between 1 and 1.3. The fitting results are listed in Table 3 and six unfolded spectra are shown in Figure 7.

### 3. Results and discussion

#### 3.1 PCA spectral fitting

The values of  $\chi^2_\nu$  ( $\chi^2_\nu = \chi^2/\text{dof}$ , refer to Table 1) and the residual distributions shown in Figure 3 show that the pca spectral fittings are statistically good. Using the same spectral model, i.e. the BB+LINE+CPL model, Church et al. (2012) fit the PCA spectra on another “Z” track of this source. In their fitting,  $\Gamma$ , i.e. photon index, is fixed at 1.7 throughout the “Z” track. In our fitting, we free this parameter in order to study its evolution. Our fitting results show that in the HB the value of  $\Gamma$  is around 1.5, basically being consistent with the fixed value of this parameter of Church et al. (2012), while it decreases remarkably in the NB and FB. In most cases of the NB and FB, the photon index is so small that its errors are relatively large, so we fix it at a relatively small value. Except  $\Gamma$ , other fitting parameters listed in Table 1 are consistent with those of Church et al. (2012) in general. The CPL component in the BB+LINE+CPL model is interpreted as the Comptonized emission of the disk soft photons inversely Comptonized by the energetic electrons from an extended ADC above the disk, while the BB component is interpreted as the emission from the NS surface (Church & Bałucińska-Church 1995, 2004). It is noted that the BB temperature spans a range of  $\sim(2.4\text{-}2.9)$  keV, as listed in Table 1, which confirm the explanation that the BB component in the BB+LINE+CPL model is from the NS, because the highest temperature of the disk, i.e. the inner disk temperature, is less than 2 keV (Mitsuda et al. 1984, 1989; Cackett et al. 2008; Lin et al. 2007, 2009; Ding et al. 2006a, 2011).

#### 3.2 HEXTE spectral fitting

we resort to the two-component model of D’Amico et al. (2001) to perform analysis for the 17 HEXTE spectra. Firstly, we use a single-component model, i.e. the BREMSS model, to fit the 17 HEXTE spectra in 20-200 keV. We find that some HEXTE spectra can be fitted statistically well by this single-component model. Six representative unfolded spectra of the single-component fitting as well as the corresponding residual distributions are shown in Figure 4. From the residual distributions shown in Figure 4 and the corresponding values of  $\chi^2_\nu$  (refer to Table 2), one can conclude that these single-component fitting are statistically acceptable. However, when six HEXTE spectra, i.e. the HEXTE spectra of HID regions 1, 4, 5, 7, 14, 15, are fitted by the BREMSS model, remarkable high-energy excesses in the energy bands above  $\sim 40$  keV are shown in the unfolded spectra or residual distributions, which are demonstrated by Figure 5. Secondly, we use the two-component model, i.e. the BREMSS+PL model, to fit the six HEXTE spectra. The fitting parameters are listed in Table 2 and the six unfolded spectra of the two-component fitting as well as the corresponding residual distributions are shown in Figure 6. Either the values of  $\chi^2_\nu$  (refer to Table 2) or the residual distributions shown in Figure 6 show that these two-component fittings are statistically good. Moreover, comparing the values of  $\chi^2$  and dof with and without the PL component in the spectral model for the six HEXTE spectra, listed in Table 2, one can conclude that the fittings are statistically better with PL than without PL, and, what is more, the fittings without the PL component are statistically unacceptable in two cases. Furthermore, the F-test probabilities for adding the PL component in the spectra model, listed in Table 2, span a range of  $\sim(10^{-2}\text{-}10^{-5})$ , which validate the PL

component in these HEXTE spectra. Our analyses suggest that a PL hard X-ray tail is detected in each of the six HEXTE spectra of HID regions 1, 4, 5, 7, 14, 15.

In any of the three branches throughout the “Z” track, the hard tail is detected in two regions. As the listed photon indices ( $\Gamma$ ) in Table 2, the hard tail continuously hardens on the HB and NB, but it softens from NB to FB, then it hardens again on the FB. The softest and hardest photon indices of the hard tail are obtained on the HB and FB, respectively. Except the photon index of region 14, the hard tail becomes hard continuously along the “Z” track in the sequence HB→NB→FB, which is consistent with hard tail behavior of Sco X-1 (D’Amico et al. 2001). The detected hard tail in region 1 contributes  $\sim 20\%$  of the total flux in the 20-200 keV energy interval. Interestingly, the ratio of the PL flux to the total flux continuously increases along the “Z” track, so that the hard tail dominates half of the total flux in region 15.

### 3.3 PCA+HEXTE spectral fitting

In order to investigate the possible mechanism for producing the hard X-ray emission in GX 17+2, we jointly fit the six PCA+HEXTE spectra in whose HEXTE spectra the hard tails are detected. Replacing the BB component in the BB+LINE+CPL model with the BMC component, this tri-component model of PCA spectral fitting turns into another tri-component model, i.e. the BMC+LINE+CPL model. We use the BMC+LINE+CPL model to fit the six PCA+HEXTE spectra in 3-200 keV. The fitting parameters are listed in Table 3 and the six unfolded spectra as well as the corresponding residual distributions are shown in Figure 7. When fitting, we find that the errors of the energy spectral index of BMC ( $\alpha$ ) are large if it is free, so we free this parameters at first and then fix it at its steady fitting value. Either the values of  $\chi^2_\nu$  (refer to Table 3) or the residual distributions shown in Figure 7 show that these spectral fittings are statistically good.

Looking at the parameters listed in Table 3 and Table 1, one can see that the LINE or CPL parameters listed in Table 3 are consistent with the corresponding LINE or CPL parameters listed in Table 1. Significantly, the BB temperatures of the seed photons for Comptonization in the BMC process, listed in Table 3, are consistent with the corresponding BB temperatures listed in Table 1 very well, indicating that the injected BB component in the BMC model is the BB component in the BB+LINE+CPL model exactly. Visibly, in each unfolded spectrum in Figure 7, the low-energy segment of the BMC component (below  $\sim 40$  keV) displays the injected BB component, while high-energy segment of the BMC component (above  $\sim 40$  keV) shows the observed Comptonization component. Looking at the red dashed lines in Figure 7 and the red dashed lines in Figure 3, one can see that the injected BB components in the BMC are just the BB components in the BB+LINE+CPL model, while the Comptonization components in the BMC fit the high-energy spectra very well. The BB component in the BB+LINE+CPL model is interpreted as the emission from the NS surface. Therefore, our analyses suggest that the BMC process taking place around the NS could be an alternative mechanism for producing the detected hard X-ray tails in GX 17+2.

## 4. Conclusion

In this work, using the *RXTE* observations for Z source GX 17+2, we study the evolution of its PCA spectra and HEXTE spectra along a complete “Z” track on its HID. In 3-30 keV, the PCA spectra can be fit by the BB+LINE+CPL model statistically well. In the HEXTE spectra, a hard X-ray tail is discontinuously detected throughout the “Z” track.

The detected hard tail hardens in the sequence HB→NB→FB in general. In the 20-200 keV energy interval, the hard tail contributes  $\sim(20-50)\%$  of the total flux. The results of jointly fitting the PCA+HEXTE spectra in 3-200 keV with the BMC+LINE+CPL model suggest that the BMC process taking place around the NS or in the boundary layer between the NS and the disk could be a mechanism for producing the hard X-ray tails.

### Acknowledgements

We thank the anonymous referee for her or his constructive comments and suggestions, which we have taken to carry out this research deeply. This research has made use of the data obtained through the High Energy Astrophysics Science Archive Research Center (HEASARC) On-line Service, provided by NASA/Goddard Space Flight Center (GSFC). This work is partially supported by National Key Basic Research Program of China (973 Program 2015CB857100), the Natural Science Foundation of China under grant nos. 11173024 and 11203064, and the Program of the Light in Chinese Western Region (LCWR) under grant no. XBBS 201121 provided by Chinese Academy of Sciences (CAS). This work is also partially supported by the 2014 Project of Xinjiang Uygur Autonomous Region of China for Flexibly Fetching in Upscale Talents.

### References

- Bałucińska-Church, M., Gibiec, A., Jackson, N. K., and Church, M. J., 2010, *Astron. Astrophys.*, **512**, A9.
- Barret, D., Olive, J. F., Boirin, L., Done, C., Skinner, G. K., and Grindlay, J. E., 2000, *Astrophys. J.*, **533**, 329.
- Cackett, E. M., Miller, J. M., Bhattacharyya, S., Grindlay, J. E., Homan, J., van der Klis, M., Miller, M. C., Strohmayer, T. E., and Wijnands, R., 2008, *Astrophys. J.*, **674**, 415.
- Church, M. J. and Bałucińska-Church, M., 1995, *Astron. Astrophys.*, **300**, 441.
- Church, M. J. and Bałucińska-Church, M., 2004, *Mon. Not. R. Astron. Soc.*, **348**, 955.
- Church, M. J., Gibiec, A., Bałucińska-Church, M., and Jackson, N. K., 2012, *Astron. Astrophys.*, **546**, A35.
- Church, M. J., Halai, G. S., and Bałucińska-Church, M., 2006, *Astron. Astrophys.*, **460**, 233.
- Coppi, P. S., 1999, in Poutanen J., Svensson R., editors, ASP Conf. Ser. Vol. 161, *High Energy Processes in Accreting Black Holes*, Page 375, Astron. Soc. Pac., San Francisco.
- D'Amico, F., Heindl, W. A., Rothschild, R. E., and Gruber, D. E., 2001, *Astrophys. J.*, **547**, L147
- D'Aí, A., Życki, P., Di Salvo, T., Iaria, R., Lavagetto, G., and Robba, N. R., 2007, *Astrophys. J.*, **667**, 411
- Ding, G. Q., Qu, J. L., and Li, T. P., 2003, *Astrophys. J.*, **596**, L219.
- Ding, G. Q., Qu, J. L., and Li, T. P., 2006a, *Astron. J.*, **131**, 1693.
- Ding, G. Q., Zhang, S. N., Li, T. p., and Qu, J. L., 2006b, *Astrophysics. J.*, **654**, 576.
- Ding, G. Q., Zhang, S. N., Wang, N., Qu, J. L., and Yan, S. P., 2011, *Astron. J.*, **142**, 34.
- Di Salvo, T., Farinelli, R., Burderi, L., Frontera, F., Kuulkers, E., Masetti, N., Robba, N. R., Stella, L., and van der Klis, M., 2002, *Astron. Astrophys.*, **386**, 535.
- Di Salvo, T., Goldoni, P., Stella, L., van der Klis, M., Bazzano, A., Burderi, L., Farinelli, R., Frontera, F., Israel, G. L., Méndez, M., and 5 coauthors, 2006, *Astrophys. J.*, **649**, L91.
- Di Salvo, T., Robba, N. R., Iaria, R., Stella, L., Burderi, L., and Israel, G. L., 2001, *Astrophys. J.*, **554**, 49.
- Di Salvo, T., Stella, L., Robba, N. R., van der Klis, M., Burderi, L., Israel, G. L., Homan, J., Campana, S., Frontera, F., and Parmar, A. N., 2000, *Astrophys. J.*, **544**, L119.
- Done, C., Gierliński, M., and Kubota, A., 2007, *Astron. Astrophys. Rev.*, **15**, 1
- Farinelli, R., Paizis, A., Landi, R., and Titarchuk, L., 2009, *Astron. Astrophys.*, **498**, 509.
- Farinelli, R., Titarchuk, L., and Frontera, F., 2007, *Astrophys. J.*, **662**, 1167.

- Farinelli, R., Titarchuk, L., Paizis, A., and Frontera, F., 2008, *Astrophys. J.*, **680**, 602.
- Fender, R. P., Dahlem, M., Homan, J., Corbel, S., Sault, R., and Belloni, T. M., 2007, *Mon. Not. R. Astron. Soc.*, **380**, L25.
- Fiocchi M., Bazzano A., Ubertini P., and Jean P., 2006, *Astrophys. J.*, **651**, 416.
- Focke, W. B., 1996, *Astrophys. J.*, **470**, L127.
- Gierliński, M., Zdziarski, A. A., Poutanen, J., Coppi, P. S., Ebisawa, K., and Johnson, W. N., 1999, *Mon. Not. R. Astron. Soc.*, **309**, 496.
- Hasinger, G., van der Klis, 1989, *Astron. Astrophys.*, **225**, 79.
- Homan, J., van der Klis, M., Jonker, P. G., Wijnands, R., Kuulkers, E., Méndez, M., and Lewin, W. H. G., 2002, *Astrophys. J.*, **568**, 878.
- Iaria, R., Burderi, L., Di Salvo, T., La Barbera, A., and Robba, N. R., 2001, *Astrophys. J.*, **547**, 412.
- Iaria, R., Di Salvo, T., Robba, N. R., and Burderi, L., 2002, *Astrophys. J.*, **567**, 503.
- Jackson, N. K., Church, M. J., and Bałucińska-Church, M., 2009, *Astron. Astrophys.*, **494**, 1059.
- Lavagetto, G., Iaria, R., Di Salvo, T., Burderi, L., Robba, N. R., Frontera, F., and Stella, L., 2004, *NuPhS*, **132**, 616.
- Laurent, P. and Titarchuk, L., 1999, *Astrophys. J.*, **511**, 289.
- Lin, D., Remillard, R. A., and Homan, J., 2007, *Astrophys. J.*, **667**, 1073.
- Lin, D., Remillard, R. A., and Homan, J., 2009, *Astrophys. J.*, **696**, 1257.
- Migliari, S., Miller-Jones, J. C. A., Fender, R. P., Homan, J., Di Salvo, T., Rothschild, R. E., Rupen, M. P., Tomsick, J. A., Wijnands, R., and van der Klis, M., 2007, *Astrophys. J.*, **671**, 706.
- Mitsuda, K., Inoue, H., Koyama, K., Makishima, K., Matsuoka, M., Ogawara, Y., Suzuki, K., Tanaka, Y., Shibazaki, N., and Hirano, T., 1984, *PASJ*, **36**, 741.
- Mitsuda, K., Inoue, H., Nakamura, N., and Tanaka, Y., 1989, *PASJ*, **41**, 97.
- Paizis, A., Farinelli, R., Titarchuk, L., Courvoisier, T. J.-L., Bazzano, A., Beckmann, V., Frontera, F., Goldoni, P., Kuulkers, E., Mereghetti, S., Rodriguez, J., and Vilhu, O., 2006, *Astron. Astrophys.*, **459**, 187.
- Penninx, W., Lewin, W. H. G., Zijlstra, A. A., Mitsuda, K., and van Paradijs, J., 1988, *Nature*, **336**, 146.
- Piraino, S., Santangelo, A., di Salvo, T., Kaaret, P., Horns, D., Iaria, R., and Burderi, L., 2007, *Astron. Astrophys.*, **471**, L17.
- Piraino S., Santangelo A., Ford E. C., and Kaaret P., 1999, *Astron. Astrophys.*, **349**, L77.
- Poutanen, J. and Coppi, P. S., 1998, *Phys. Scr.*, **T77**, 57.
- Raichur, H., Misra, R., and Dewangan, G., 2011, *Mon. Not. R. Astron. Soc.*, **416**, 637.
- Revnivtsev, M. G., Tsygankov, S. S., Churazov, E. M., and Krivonos, R. A., 2014, *Mon. Not. R. Astron. Soc.*, **445**, 1205.
- Riegler, G. R., 1970, *Nature*, **226**, 1041.
- Shapiro, S. L., Lightman, A. P., and Eardley, D. M., 1976, *Astrophys. J.*, **204**, 187.
- Shrader, C. and Titarchuk, L., 1998, *Astrophys. J.*, **499**, L31.
- Sunyaev, R. A. and Truemper, J., 1979, *Nature*, **279**, 506.
- Sunyaev, R. A. and Titarchuk, L. G., 1980, *Astron. Astrophys.*, **86**, 121.
- Tarana A., Bazzano A., Ubertini P., and Zdziarski A. A., 2007, *Astrophys. J.*, **654**, 494.
- Tarana A., Belloni T., Bazzano A., Méndez M., and Ubertini P., 2011, *Mon. Not. R. Astron. Soc.*, **416**, 873.
- Titarchuk, L., 1994, *Astrophys. J.*, **434**, 570.
- Titarchuk, L., Mastichiadis, A., and Kylafis, N. D., 1996, *Astron. Astrophys. Supp.*, **120**, 171.
- Titarchuk, L., Mastichiadis, A., and Kylafis, N. D., 1997, *Astrophys. J.*, **487**, 834.
- Titarchuk, L. and Seifina, E., 2009, *Astrophys. J.*, **706**, 1463.
- White, N. E., Peacock, A., Hasinger, G., Mason, K. O., Manzo, G., Taylor, B. G., and Branduardi-Raymont, G., 1986, *Mon. Not. R. Astron. Soc.*, **218**, 129.
- White, N. E., Stella, L., and Parmar, A. N., 1988, *Astrophys. J.*, **324**, 363.
- Zdziarski, A. A., Grove, J. E., Poutanen, J., Rao, A. R., and Vadawale, S. V., 2001, *Astrophys. J.*, **554**, L45.

**Table 1.** The spectral fitting parameters of PCA spectra in 3-30 keV for the HID regions of GX 17+2, using a model consisting of a BB, a LINE, and a CPL. Errors quoted are 90% confidence limits for the fitting parameters ( $\Delta\chi^2 = 2.7$ ).

HID (No.)	BB			LINE			CPL			$\chi^2$ (dof)
	$^a N_H$ ( $\times 10^{-22}$ )	$kT_{\text{bb}}$ (keV)	$N_{\text{bb}}$	$E_{\text{Fe}}$ (keV)	$^b EW$ (eV)	$N_{\text{Fe}}$ ( $\times 10^{-2}$ )	$^c \Gamma$	$E_{\text{cut}}$ (keV)	$N_{\text{cpl}}$	
HB										
1	$3.22^{+0.46}_{-0.42}$	$2.80^{+0.09}_{-0.06}$	$7.5^{+1.6}_{-1.5}$	$6.48^{+0.05}_{-0.05}$	96	$1.6^{+0.3}_{-0.2}$	$1.57^{+0.19}_{-0.17}$	$7.4^{+1.0}_{-0.8}$	$5.9^{+1.4}_{-1.0}$	34.3(42)
2	$3.15^{+0.44}_{-0.32}$	$2.82^{+0.09}_{-0.08}$	$6.1^{+1.6}_{-1.1}$	$6.48^{+0.05}_{-0.05}$	83	$1.4^{+0.3}_{-0.2}$	$1.42^{+0.18}_{-0.13}$	$6.3^{+0.8}_{-0.5}$	$5.6^{+0.8}_{-0.7}$	43.8(42)
3	$4.18^{+0.53}_{-0.42}$	$2.72^{+0.09}_{-0.08}$	$7.5^{+1.9}_{-1.4}$	$6.44^{+0.07}_{-0.08}$	115	$2.1^{+0.7}_{-0.4}$	$1.63^{+0.22}_{-0.17}$	$6.3^{+0.9}_{-0.6}$	$8.7^{+2.4}_{-1.5}$	45.3(42)
4	$4.08^{+0.33}_{-0.35}$	$2.74^{+0.10}_{-0.07}$	$6.0^{+1.2}_{-1.0}$	$6.46^{+0.06}_{-0.07}$	101	$1.9^{+0.4}_{-0.4}$	$1.46^{+0.13}_{-0.14}$	$5.4^{+0.4}_{-0.5}$	$7.9^{+1.3}_{-1.1}$	37.5(42)
NB										
5	$3.78^{+0.37}_{-0.50}$	$2.86^{+0.11}_{-0.13}$	$4.2^{+0.9}_{-0.5}$	$6.46^{+0.06}_{-0.07}$	92	$1.8^{+0.5}_{-0.4}$	$1.19^{+0.16}_{-0.30}$	$4.5^{+0.5}_{-0.8}$	$6.6^{+1.2}_{-1.4}$	44.7(42)
6	$3.66^{+0.49}_{-0.62}$	$2.88^{+0.02}_{-0.07}$	$4.8^{+2.7}_{-1.1}$	$6.46^{+0.06}_{-0.06}$	88	$1.6^{+0.4}_{-0.3}$	$0.95^{+0.28}_{-0.40}$	$3.5^{+0.8}_{-0.8}$	$6.0^{+1.5}_{-1.5}$	37.5(42)
7	$3.08^{+0.13}_{-0.13}$	$2.83^{+0.03}_{-0.03}$	$5.5^{+0.5}_{-0.5}$	$6.44^{+0.05}_{-0.05}$	77	$1.4^{+0.3}_{-0.2}$	0.60(fixed)	$2.8^{+0.1}_{-0.1}$	$4.5^{+0.2}_{-0.2}$	46.5(43)
8	$3.07^{+0.13}_{-0.13}$	$2.79^{+0.03}_{-0.04}$	$5.2^{+0.6}_{-0.5}$	$6.48^{+0.04}_{-0.05}$	109	$1.7^{+0.3}_{-0.2}$	0.50(fixed)	$2.6^{+0.1}_{-0.1}$	$4.3^{+0.2}_{-0.2}$	44.7(43)
9	$3.47^{+0.78}_{-0.76}$	$2.72^{+0.13}_{-0.09}$	$4.7^{+2.2}_{-2.4}$	$6.50^{+0.03}_{-0.04}$	172	$2.5^{+0.4}_{-0.3}$	$0.61^{+0.48}_{-0.45}$	$2.6^{+0.8}_{-0.5}$	$4.8^{+2.1}_{-1.5}$	41.1(42)
FB										
10	$3.16^{+0.14}_{-0.15}$	$2.78^{+0.06}_{-0.06}$	$3.7^{+0.7}_{-0.7}$	$6.51^{+0.03}_{-0.04}$	193	$2.9^{+0.3}_{-0.3}$	0.50(fixed)	$2.6^{+0.1}_{-0.1}$	$4.1^{+0.2}_{-0.2}$	66.4(43)
11	$3.24^{+0.14}_{-0.14}$	$2.77^{+0.05}_{-0.05}$	$4.3^{+0.9}_{-0.7}$	$6.49^{+0.03}_{-0.04}$	189	$3.2^{+0.3}_{-0.3}$	0.50(fixed)	$2.7^{+0.1}_{-0.1}$	$4.1^{+0.2}_{-0.2}$	52.0(43)
12	$3.25^{+0.14}_{-0.14}$	$2.85^{+0.07}_{-0.06}$	$3.5^{+0.8}_{-0.8}$	$6.52^{+0.03}_{-0.04}$	169	$3.2^{+0.3}_{-0.3}$	0.50(fixed)	$2.9^{+0.1}_{-0.1}$	$4.0^{+0.2}_{-0.2}$	63.6(43)
13	$3.27^{+0.15}_{-0.14}$	$2.80^{+0.06}_{-0.06}$	$4.1^{+1.4}_{-1.0}$	$6.51^{+0.04}_{-0.04}$	166	$3.5^{+0.4}_{-0.3}$	0.50(fixed)	$3.1^{+0.1}_{-0.1}$	$4.0^{+0.2}_{-0.2}$	59.6(43)
14	$3.13^{+0.15}_{-0.15}$	$2.75^{+0.07}_{-0.16}$	$2.2^{+1.6}_{-1.4}$	$6.48^{+0.04}_{-0.05}$	142	$3.5^{+0.5}_{-0.4}$	0.50(fixed)	$3.5^{+0.1}_{-0.1}$	$3.8^{+0.2}_{-0.2}$	40.3(43)
15	$3.22^{+0.17}_{-0.17}$	$2.50^{+0.16}_{-0.36}$	$4.9^{+1.5}_{-1.1}$	$6.51^{+0.06}_{-0.06}$	141	$3.9^{+0.8}_{-0.7}$	0.50(fixed)	$3.7^{+0.2}_{-0.2}$	$3.8^{+0.2}_{-0.2}$	63.5(43)
16	$2.92^{+0.16}_{-0.17}$	$2.42^{+0.09}_{-0.10}$	$12.7^{+1.8}_{-1.3}$	$6.47^{+0.06}_{-0.06}$	120	$3.7^{+0.7}_{-0.6}$	0.50(fixed)	$3.9^{+0.1}_{-0.1}$	$3.6^{+0.2}_{-0.2}$	44.6(43)
17	$2.92^{+0.19}_{-0.19}$	$2.49^{+0.06}_{-0.06}$	$21.9^{+1.5}_{-1.4}$	$6.51^{+0.07}_{-0.07}$	84	$2.8^{+0.5}_{-0.4}$	0.50(fixed)	$4.0^{+0.1}_{-0.2}$	$3.7^{+0.2}_{-0.2}$	29.9(43)

<sup>a</sup>The interstellar hydrogen column density.

<sup>b</sup>The equivalent width of the line component.

<sup>c</sup>The photon index of the CPL component.

**Table 2.** The spectral fitting parameters of the HEXTE spectra in 20-200 keV, using a two-component model consisting of a BREMSS, plus a PL, or a one-component model of BREMSS. Errors quoted are 90% confidence limits for the fitting parameters ( $\Delta\chi^2 = 2.7$ ).

HID (No.)	BREMSS		PL		$\chi^2$ (dof)	${}^c\chi^2$ (dof)	${}^dF$ -test
	$kT$ (keV)	${}^a$ Flux	$\Gamma$	${}^b$ Flux			
<b>HB</b>							
1	$6.28^{+0.44}_{-0.74}$	$1.17^{+0.28}_{-0.43}$	$1.37^{+0.58}_{-0.62}$	$0.32^{+0.21}_{-0.12}$	6.19(14)	18.08(16)	$5.5 \times 10^{-4}$
2	$6.24^{+0.19}_{-0.19}$	$1.05^{+0.02}_{-0.02}$	—	—	12.71(11)	—	—
3	$5.84^{+0.22}_{-0.21}$	$0.85^{+0.02}_{-0.02}$	—	—	19.04(12)	—	—
4	$5.50^{+0.16}_{-0.17}$	$0.74^{+0.02}_{-0.02}$	$0.60^{+0.52}_{-0.45}$	$0.26^{+0.09}_{-0.08}$	14.87(16)	47.60(18)	$9.1 \times 10^{-5}$
<b>NB</b>							
5	$5.33^{+0.17}_{-0.17}$	$0.63^{+0.02}_{-0.02}$	$0.22^{+0.15}_{-0.18}$	$0.33^{+0.09}_{-0.09}$	10.58(8)	58.51(10)	$1.1 \times 10^{-3}$
6	$4.75^{+0.15}_{-0.15}$	$0.48^{+0.02}_{-0.02}$	—	—	8.97(11)	—	—
7	$5.02^{+0.26}_{-0.26}$	$0.42^{+0.02}_{-0.02}$	$-0.16^{+0.14}_{-0.12}$	$0.18^{+0.11}_{-0.11}$	7.00(9)	15.16(11)	$3.1 \times 10^{-2}$
8	$4.67^{+0.32}_{-0.30}$	$0.32^{+0.02}_{-0.02}$	—	—	11.55(11)	—	—
9	$4.41^{+0.32}_{-0.29}$	$0.24^{+0.02}_{-0.02}$	—	—	10.95(11)	—	—
<b>FB</b>							
10	$4.40^{+0.56}_{-0.48}$	$0.24^{+0.02}_{-0.02}$	—	—	14.95(13)	—	—
11	$4.46^{+0.44}_{-0.39}$	$0.30^{+0.02}_{-0.02}$	—	—	12.39(13)	—	—
12	$4.14^{+0.33}_{-0.30}$	$0.33^{+0.02}_{-0.02}$	—	—	16.72(12)	—	—
13	$4.12^{+0.26}_{-0.24}$	$0.40^{+0.02}_{-0.02}$	—	—	8.64(10)	—	—
14	$4.35^{+0.42}_{-0.51}$	$0.54^{+0.04}_{-0.09}$	$0.89^{+0.65}_{-0.73}$	$0.36^{+0.24}_{-0.19}$	7.27(10)	19.51(12)	$7.2 \times 10^{-3}$
15	$4.57^{+0.49}_{-0.50}$	$0.72^{+0.05}_{-0.07}$	$-0.33^{+0.28}_{-0.30}$	$0.72^{+0.38}_{-0.39}$	5.31(6)	15.83(8)	$3.8 \times 10^{-2}$
16	$4.45^{+0.31}_{-0.28}$	$0.93^{+0.04}_{-0.04}$	—	—	14.78(12)	—	—
17	$4.91^{+0.43}_{-0.39}$	$1.29^{+0.07}_{-0.07}$	—	—	5.93(12)	—	—

<sup>a</sup>The unabsorbed flux in the 20-50 keV range in units of  $10^{-9}$  ergs  $\text{cm}^{-1}$   $\text{s}^{-1}$

<sup>b</sup>The unabsorbed flux in the 20-200 keV range in units of  $10^{-9}$  ergs  $\text{cm}^{-1}$   $\text{s}^{-1}$

<sup>c</sup>The  $\chi^2$  and degree of freedom when the PL component is not included in the spectral model

<sup>d</sup>The probability of chance improvement when a PL is included in the spectral model

**Table 3.** The spectral fitting parameters of the PCA+HEXTE spectra in which a hard tail is detected. The spectra are fit in 3-200 keV, with the model consisting of a BMC, a LINE, and a CPL. Errors quoted are 90% confidence limits for the fitting parameters ( $\Delta\chi^2 = 2.7$ ).

HID (No.)	BMC				LINE			CPL			$f$	$\chi^2$ (dof)	
	$^a N_H$	$kT_{\text{bb}}$ (keV)	$^b \alpha$	$\log(A)$	$N_{\text{bmc}}$ ( $\times 10^{-2}$ )	$E_{\text{Fe}}$ (keV)	$^c EW$ (eV)	$N_{\text{Fe}}$ ( $\times 10^{-2}$ )	$^d \Gamma$	$E_{\text{cut}}$ (keV)			$N_{\text{cpl}}$
<b>HB</b>													
1	$3.3^{+0.5}_{-0.4}$	$2.8^{+0.1}_{-0.1}$	0.01(fixed)	$-0.58^{+0.18}_{-0.31}$	$7.8^{+0.9}_{-0.9}$	$6.5^{+0.1}_{-0.1}$	97	$1.6^{+0.3}_{-0.2}$	$1.6^{+0.2}_{-0.2}$	$7.4^{+1.2}_{-0.9}$	$6.1^{+1.7}_{-1.1}$	21%	39.4(52)
4	$4.4^{+0.5}_{-0.4}$	$2.7^{+0.1}_{-0.1}$	0.01(fixed)	$-0.64^{+0.12}_{-0.16}$	$5.8^{+0.6}_{-0.5}$	$6.5^{+0.1}_{-0.1}$	111	$2.1^{+0.6}_{-0.4}$	$1.6^{+0.2}_{-0.2}$	$5.8^{+0.7}_{-0.5}$	$9.1^{+2.2}_{-1.4}$	19%	57.7(53)
<b>NB</b>													
5	$3.2^{+0.2}_{-0.2}$	$2.9^{+0.1}_{-0.1}$	0.01(fixed)	$-0.69^{+0.08}_{-0.10}$	$7.2^{+0.5}_{-0.5}$	$6.5^{+0.1}_{-0.1}$	81	$1.5^{+0.3}_{-0.2}$	0.8(fixed)	$3.2^{+0.1}_{-0.1}$	$4.9^{+0.2}_{-0.2}$	17%	56.6(48)
7	$3.1^{+0.2}_{-0.2}$	$2.8^{+0.1}_{-0.1}$	0.01(fixed)	$-0.88^{+0.17}_{-0.29}$	$5.4^{+0.5}_{-0.5}$	$6.4^{+0.1}_{-0.1}$	80	$1.4^{+0.3}_{-0.2}$	0.6(fixed)	$2.8^{+0.1}_{-0.1}$	$4.6^{+0.2}_{-0.2}$	12%	53.4(48)
<b>FB</b>													
14	$3.1^{+0.2}_{-0.2}$	$2.7^{+0.1}_{-0.2}$	0.01(fixed)	$-0.15^{+0.33}_{-0.28}$	$3.4^{+0.9}_{-0.8}$	$6.5^{+0.1}_{-0.1}$	142	$3.5^{+0.5}_{-0.4}$	0.5(fixed)	$3.5^{+0.2}_{-0.2}$	$3.8^{+0.2}_{-0.1}$	41%	46.2(49)
15	$3.3^{+0.2}_{-0.2}$	$2.6^{+0.1}_{-0.2}$	0.01(fixed)	$-0.27^{+0.20}_{-0.28}$	$5.5^{+1.5}_{-1.2}$	$6.5^{+0.1}_{-0.1}$	145	$4.0^{+0.9}_{-0.7}$	0.5(fixed)	$3.6^{+0.2}_{-0.2}$	$3.9^{+0.3}_{-0.2}$	35%	67.4(45)

<sup>a</sup>The interstellar hydrogen column density, in units of  $10^{-22} \text{ cm}^2$ .

<sup>b</sup>The energy spectral index of BMC ( $\Gamma_1 = \alpha + 1$ )

<sup>c</sup>The equivalent width of the line component.

<sup>d</sup>The photon index of the CPL component.

<sup>e</sup>The Comptonization factor of BMC:  $f = A/(A+1)$

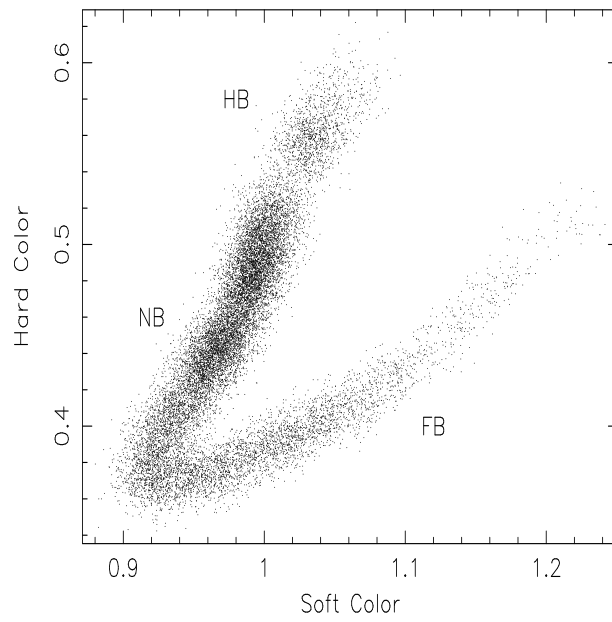


**Figure 1.** The CD of GX 17+2. Each point represents 16 s background-subtracted data. The soft color is defined as the count rate ratio between 4.6–7.1 keV and 2.9–4.6 keV energy bands, while the hard color is defined as the count rate ratio between 10.5–19.6 and 7.1–10.5 energy bands.

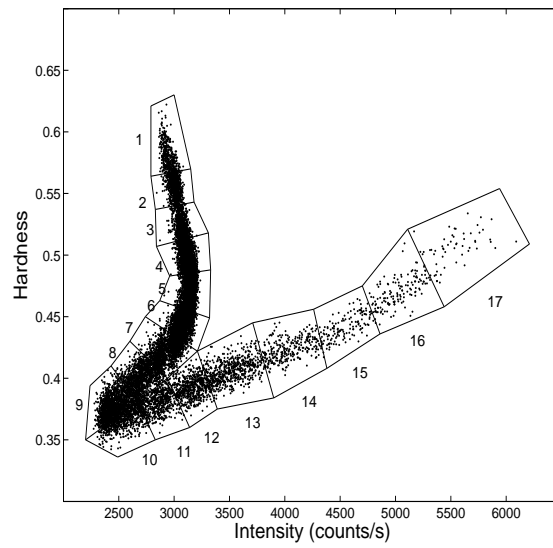


**Figure 2.** The HID of GX 17+2, which is divided into seventeen regions as labeled. Each point represents 16 s background-subtracted data. The hardness is defined as the count rate ratio between 10.5–19.6 keV and 7.1–10.5 keV energy bands, and the intensity is defined as the count rate in 2.9–19.6 keV.

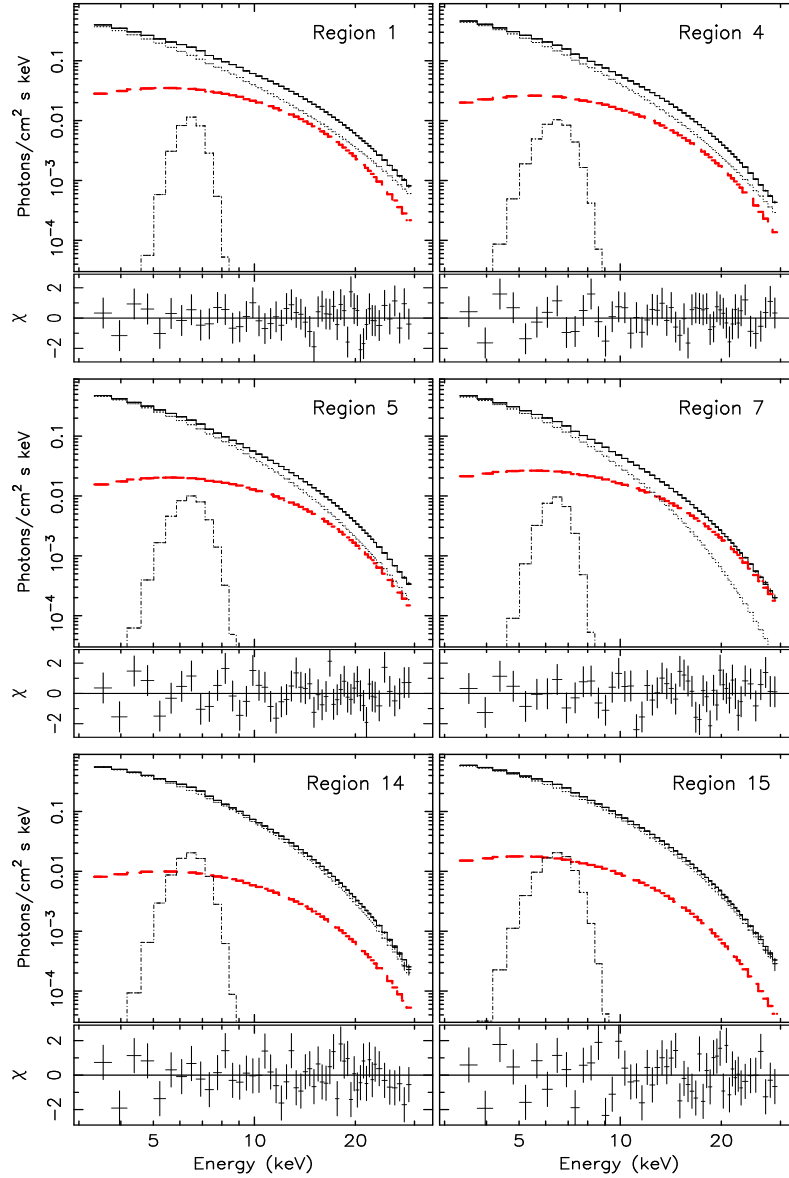


**Figure 3.** Six unfolded spectra of PCA spectral fitting in 3-30 keV, showing three individual components, namely, BB (red dashed line), LINE (dot-dashed line), and CPL (dotted line). The residuals ( $\chi$ ) in terms of  $\sigma$  with error bar for each spectral fitting are demonstrated. The residual distributions show that these fittings are statistically good.

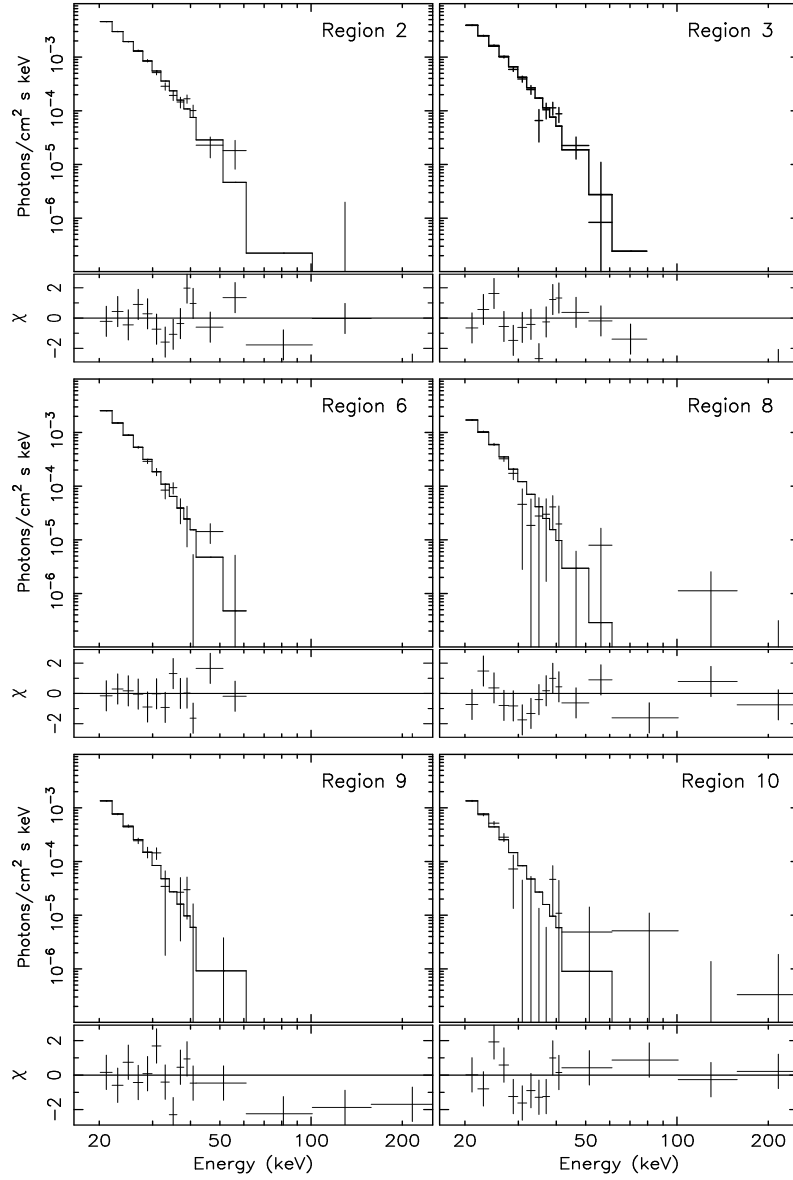


**Figure 4.** Six unfolded spectra of HEXTE spectral fitting in 20-200 keV, showing an individual component, namely, BREMSS (solid line). The residuals ( $\chi$ ) in terms of  $\sigma$  with error bar for each spectral fitting are demonstrated. The residual distributions show that these fittings are statistically acceptable.

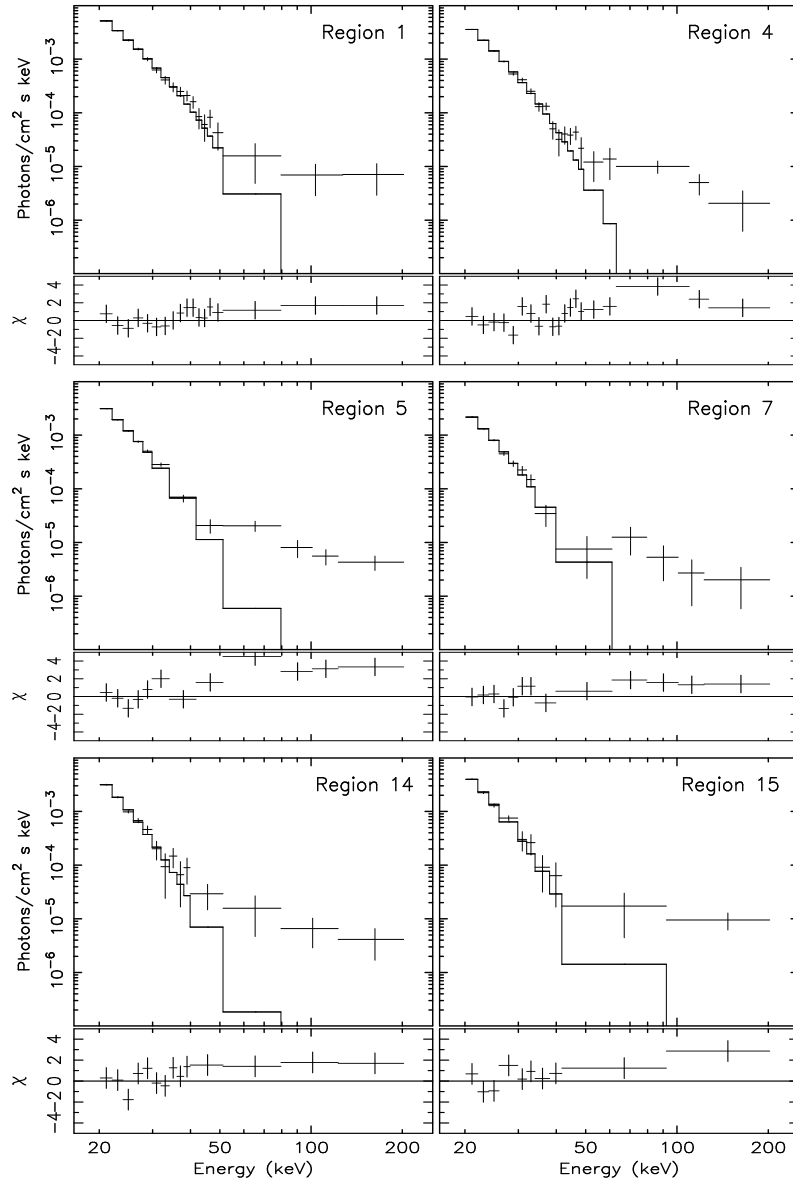


**Figure 5.** Six unfolded spectra of HEXTE spectral fitting in 20-200 keV, showing an individual component, namely, BREMSS (solid line). The residuals ( $\chi$ ) in terms of  $\sigma$  with error bar for each spectral fitting are demonstrated. Either these unfolded spectra or residual distributions show that there are obvious high-energy excesses in the energy bands higher than  $\sim 40$  keV.

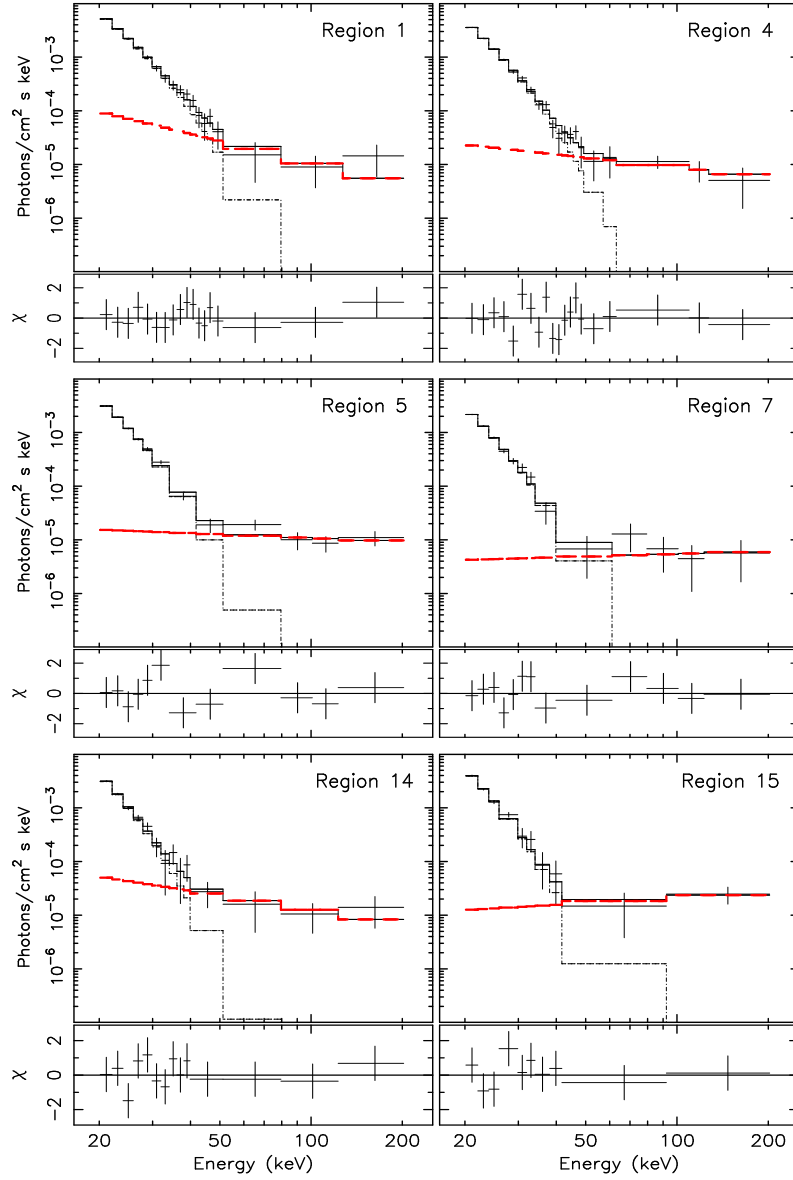


**Figure 6.** Six unfolded spectra of HEXTE spectral fitting in 20-200 keV, showing two individual components, namely, BREMSS (dot-dashed line) and PL (red dashed line). The residuals ( $\chi$ ) in terms of  $\sigma$  with error bar for each spectral fitting are demonstrated. The residual distributions show that these fittings are statistically good.

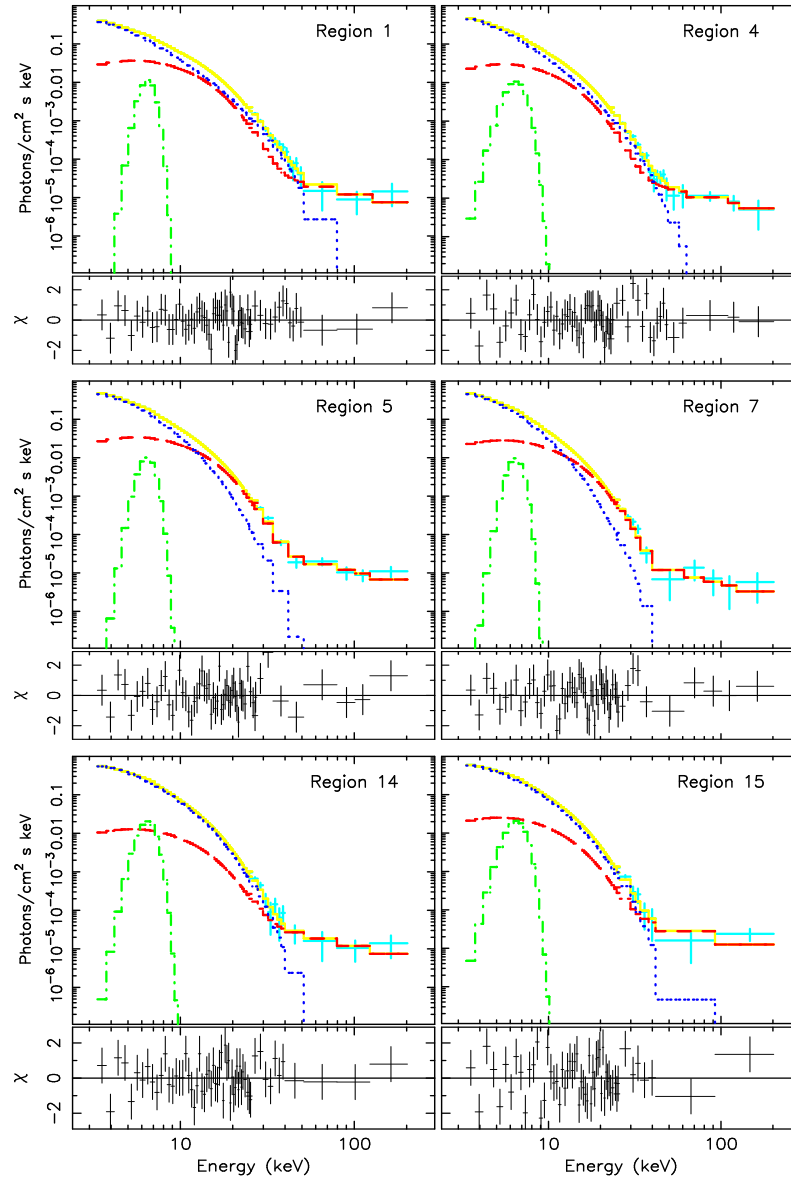


**Figure 7.** Six unfolded spectra of PCA+HEXTE spectral fitting in 3-200 keV, in which hard tails are detected, showing three individual components, namely, BMC (red dashed line), LINE (green dot-dashed line), and CPL (blue dotted line), as well as the sum of individual components (solid yellow line) and the data (celeste crosses). The residuals ( $\chi$ ) in terms of  $\sigma$  with error bar for each spectral fitting are demonstrated. The residual distributions show that these fittings are statistically good.